Journal of Thermal Analysis and Calorimetry (2025) 150:1657–1667
https://doi.org/10.1007/s10973-024-13948-1

Investigation on nanocrystallization, thermal stability and hardness of amorphous $Al_{86}Cu_6Y_6Co_2$ alloy

M. Salehi[1] · **S. G. Shabestari**[1] · **M. Dadashi**[1]

Received: 22 December 2023 / Accepted: 7 December 2024 / Published online: 19 January 2025

Abstract
In this study, nanocrystallization behavior, thermal stability, mechanical properties, and intermetallics formation of $Al_{86}Cu_6Y_6Co_2$ (at.%) as-spun amorphous ribbons were investigated by X-ray diffraction (XRD), differential scanning calorimetry (DSC), field emission scanning electron microscopy (FE-SEM) and microhardness. Kissinger, Ozawa, and Augis- Bennett methods were used to study the kinetics of crystallization. Activation energies for primary crystallization of the amorphous alloy in non-isothermal conditions using these methods (173–178 $kJmol^{-1}$) indicate a relatively high thermal stability. The mean amount of Avrami index (~ 2.1) revealed the first stage reaction is controlled by a 3-D diffusional growth with a reducing nucleation rate. The α-Al nanoparticles and intermetallic phases are embedded evenly into the glassy matrix during the first (623 K) and second reactions (723 K), respectively. The maximum microhardness of about 310 Hv is achieved in the $Al_{86}Cu_6Y_6Co_2$ alloy annealed at 623 K due to the enhancement of the solute content and the effect of α-Al nanocrystals.

Keywords Nanostructures · Alloys · Rare earth compounds · Characterization · Solidification · Nucleation

Introduction

The rapid solidification process has noticeable profits compared to the conventional casting processes which led to a higher demand for advanced materials. Recently, there is a large interest to produce Al alloys by rapid solidification [1–4]. Metallic glasses with excellent properties, which make them a good choice for different advanced applications, can be produced by a rapid solidification process [5–7].

Transition metal (TM) and rare earth (RE) elements have been used with high content of Al (> 80 at.%) in order to produce amorphous Al (rich) -TM-RE alloys which were investigated intensively because of their unique mechanical properties and high glass-forming ability (GFA). Al amorphous alloys represent a tensile strength of about 1000 MPa, good ductility, hardness, wear, and corrosion resistance [8–12].

Al-based alloys as marginal glass formers need more cooling rates (10^5–10^6 Ks^{-1}) to bypass devitrification. Rapid solidification methods like melt spinning are essential to produce amorphous structures [11, 13–15]. The monolithic metallic glasses show low ductility because of the local plastic deformation in shear bands, resulting in sudden failure. Therefore, a nanocrystalline-amorphous composite material has been introduced to overcome such a fundamental problem [15]. There are many routes to form these composites from metallic glasses among them; heat treatment has attracted more attention due to better control of the process [16]. Homogeneously distributed nano-sized fcc α-Al particles in the amorphous matrix enhance even more the mechanical properties after partial crystallization. These nanocrystals increase ductility by increasing the number of the shear bands and suppressing their spreading [15, 17–19]. Besides, the enhancement of the solute content of the remaining glassy matrix, or considering both parameters of the α-Al nanoparticles and the remaining glassy matrix result in high mechanical properties of the alloy [10]. The behavior of these amorphous-nanocrystalline composites gets brittle after the formation of the intermetallic phases. Therefore, studying the first devitrification, thermal stability, and glass-forming ability (GFA) of Al-based metallic glasses has great importance [20, 21]. The controlled crystallization that results in fine microstructures is critical to increasing their mechanical properties.

✉ M. Salehi
maryamsalehi@iust.ac.ir

[1] School of Metallurgy and Materials Engineering, Iran University of Science and Technology (IUST), Tehran, Iran

Isothermal and non-isothermal are two routes that are used to determine the mechanism of crystallization. In an isothermal approach, the instrument keeps at the desired temperature for a while then the reaction events collect, in the non-isothermal approach the temperature increases isochronal. As the non-isothermal methods are faster and have the ability to apply higher temperatures, they have been recently intensively studied. In addition, the thermal history has no effect on the non-isothermal routes [8, 22].

Although many studies have been done on the Al-Ni-RE metallic glasses [7–9, 13, 20], there are few in the fields of Al-Cu-RE alloys with high casting and mechanical properties. Therefore, in this study, the non-isothermal devitrification and determination of each crystallization product of $Al_{86}Cu_6Y_6Co_2$ (at.%) metallic glass were studied. In order to determine the mechanism of the crystallization process through a comprehensive study of the crystallization kinetics, various methods have been applied to determine the crystallization activation energies and the precision of each technique has been discussed. The fraction of the crystalline phases is related to the annealing temperature. In addition, the relation between the mechanical properties and crystalline phases related to each reaction stage in heat-treated Al amorphous alloy was analyzed. For this purpose, microhardness tests have been applied for samples at as-spun and annealed conditions, and the effect of microstructural changes after each crystallization reaction on the microhardness is discussed.

Experimental

Materials and melt spinning technique

Ingot of $Al_{86}Cu_6Y_6Co_2$ alloy (atomic nominal composition) was produced using high-frequency induction melting under a high-purity Ar atmosphere, repeated three times to obtain a homogeneous composition. All the elements used were pure metals (purity > 99.9%). A melt spinning device with the speed of 40 ms^{-1} was used for the as-cast sample under an Ar atmosphere to produce amorphous melt-spun ribbons. The machine consists of a melting system and a spinning copper wheel. After melting in a nozzle, the alloy was poured on the surface of a spinning wheel (32 cm diameter). The spinning operation produced ribbons with a typical thickness of 15–22 μm, a width of 1–1.5 mm, and a length of more than 2 m.

Structural characterization

The non-isothermal crystallization behavior, GFA, and thermal stability of the rapidly solidified ribbons have been studied using differential scanning calorimetry (DSC- Mettler Toledo). About 2 mg of the specimen were annealed inside the DSC instrument up to 873 K under an Ar atmosphere and heating rates of 10, 20, and 30 $Kmin^{-1}$. The crystallization activation energies can be determined through the changes in the transition temperatures of the amorphous alloy during thermal analysis at various heating rates. Moreover, in order to determine phases formed during the crystallization steps, the amorphous alloy was annealed to the temperatures corresponding to the end position of each reaction peak at a 20 $Kmin^{-1}$ heating rate. The specimens were then rapidly cooled preventing extra crystallization. X-ray diffraction (XRD-Philips, PW1800) at 2θ range from 10◦ to 80◦ (CuK_α, 40 kV, 20 mA) was used to study the phase evolution of the amorphous and heat-treated samples. The distribution and morphology of the crystalline phases were investigated by KYKY-EM 8000F field emission scanning electron microscope (FE-SEM) at a voltage of 15 kV which was also attached to an energy-dispersive spectrometry (EDS Silicon Drift 2017). The specimens were mounted from longitudinal. A modified Keller's solution has been used for about 5 s. MVK-H21 microhardness tester with the accuracy of + 3.75% has been used to determine the hardness of the samples. The measurements have been done on the longitudinal sections of the ribbons and at the applied load of 25 g. Eight microhardness measurements have been done on each sample and the average amounts were reported.

Results

Figure 1a reveals the XRD pattern of the rapidly solidified $Al_{86}Cu_6Y_6Co_2$ (at. %) alloy. As illustrated, a wide diffraction peak at 2θ range of 32–48° has been formed and there is no sharp peak in the XRD pattern corresponding to the crystalline phases. Therefore, the ribbons of the as-spun $Al_{86}Cu_6Y_6Co_2$ (at. %) alloy are fully amorphous. Figure 2 shows the isochronal DSC curves of the rapidly solidified alloy at 10 $Kmin^{-1}$, 20 $Kmin^{-1}$, and 30 $Kmin^{-1}$ heating rates. The curves consist of two specific exothermic crystallization peaks. Therefore, the ribbons show a two-stage crystallization reaction. However, it seems that there is a small peak between the first and second sharp peaks. This peak is specified more at the heating rate of 30 $Kmin^{-1}$. The crystallization is quite sensitive to composition. Most Al-TM-RE alloys crystallize in the three stages, but there are some cases that only show two stages. Moreover, the heating rate in the DSC experiments influences the transformation temperatures and the ability to detect the transformations, especially in the case, they are very close to each other [8, 10]. Only some of the Al metallic glasses demonstrate the glass transition phenomenon [23]. However, glass transition, a small endothermic signal, can be observed in the studied alloy. In Table 1, the transition temperatures (T_g, T_{X1}, T_{X2},

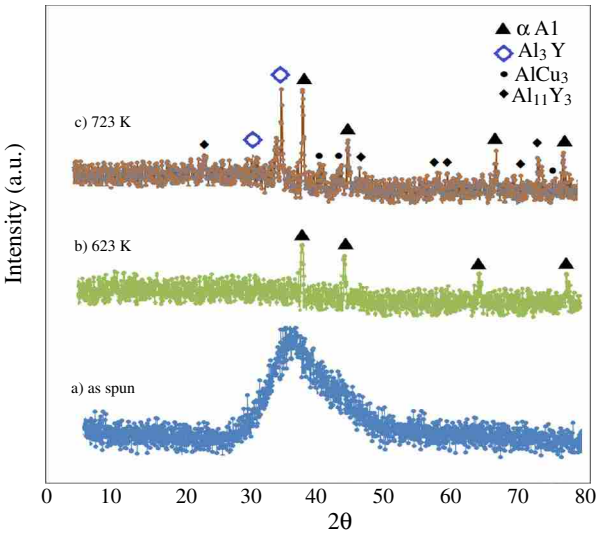

Fig. 1 Different conditions in XRD patterns of the $Al_{86}Cu_6Y_6Co_2$ ribbons: (**a**) as-solidified ribbons and (**b** and **c**) samples heating up to 623 K and 723 K (20 $Kmin^{-1}$) related to each crystallization stage revealing various phase evolution during annealing

T_{P1}, T_{P2}) and supercooled liquid region ($\Delta T_{X1} = T_{X1}\text{-}T_g$) at 10- 30 $Kmin^{-1}$ heating rates are reported. Transition temperatures of the DSC curves and their intensity increase with increasing heating rates. The relaxation of the amorphous alloy leads to a transition temperature peak of T_g in the DSC curves. Also, as the crystallization is a thermally activated process, the transition temperatures advance with the increasing of the heating rates [24].

The results show that the $Al_{86}Cu_6Y_6Co_2$ amorphous alloy demonstrates higher transition temperatures with respect to $Al_{86}Ni_6Y_6Ce_2$ amorphous alloy with the same Al atomic percent, and it is comparable to $Al_{84}Ni_6Y_6Ce_4$ glassy alloy [17] indicating high thermal stability of the studied ribbons.

The $Al_{86}Cu_6Y_6Co_2$ ribbons annealed at the end temperature of each reaction have been studied by the XRD analysis to determine the phases which form during the crystallization. For this purpose, the melt-spun ribbons were annealed in the range of 623–723 K and 20 $Kmin^{-1}$ heating rate. From isochronal DSC curves (Fig. 2), the temperature and time of annealing were estimated. The results indicate that the fcc α-Al nanoparticles are precipitated during the first DSC reaction (Fig. 1b); whereas, the XRD result of the alloy after complete crystallization is assigned to the intermetallic phases formation, Al_3Y, $AlCu_3$, $Al_{11}Y_3$ phases and some unidentified phases observed at 723 K (Fig. 1c). The fcc α-Al nanocrystals growth throughout the second crystallization can be defined from the more peak intensity of the α-Al phase.

Figure 3 shows FE-SEM images of as-spun amorphous $Al_{86}Cu_6Y_6Co_2$ (at. %) alloy and samples continuously heated

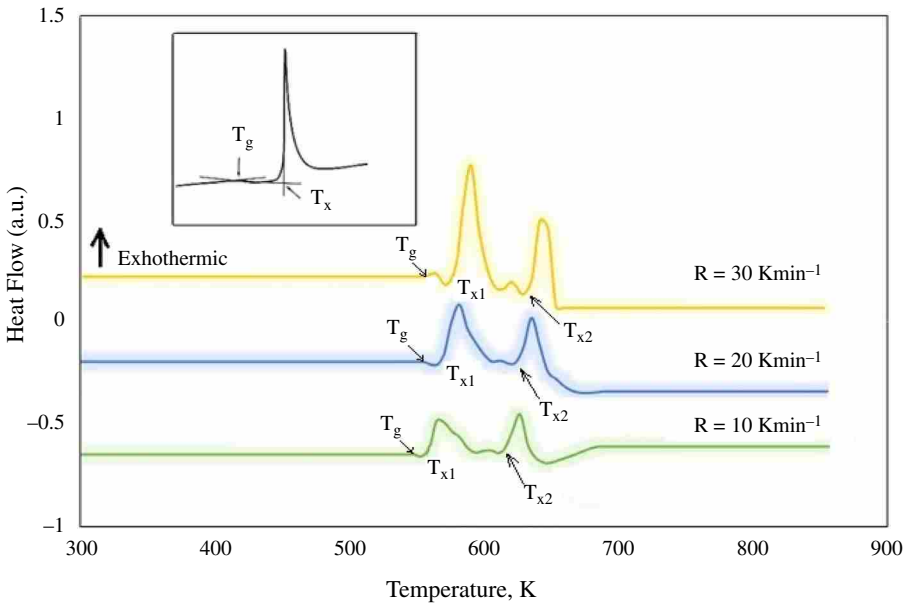

Fig. 2 DSC curves of $Al_{86}Cu_6Y_6Co_2$ (at. %) amorphous alloy with a two stages crystallization reaction at 10- 30 $Kmin^{-1}$ heating rates

Table 1 Transition temperatures of $Al_{86}Cu_6Y_6Co_2$ (at. %) as-spun ribbons

ΔT_x	K/T_{p2}	K/T_{p1}	K/T_{x2}	K/T_{x1}	K/T_g	K/min/β
26	642	574	632	566	540	10
24	653	584	769	576	552	20
23	662	591	652	582	559	30

to 623 K and 723 K (the end temperature of each reaction). As can be seen from Fig. 3a, the as-spun alloy shows an amorphous structure. This is in accordance with the XRD results of the melt-spun ribbon shown in Fig. 1a. An example obtained for the $Al_{86}Cu_6Y_6Co_2$ amorphous alloy annealed to 623 K is shown in Fig. 3b. It is quite clear that a high-density of the nanometer scale α-Al crystals with a globular geometry are dispersed in the as-prepared amorphous matrix. The EDS pattern (Fig. 3d) shows the precipitation of α-Al. However, EDS analysis due to the effect of matrix composition in the analysis of small phases is rather inaccurate. The fine bright phases have been considered to be fcc α-Al nanocrystals (Fig. 3d) which are in accordance with the XRD analysis (Fig. 1b). Large Y atoms lead to a decrease in the diffusion at fronts of the crystal growth and suppression of more growth of the α-Al nanoparticles; therefore, a nanocrystalline (fcc-Al)-amorphous composite has been formed. The heat treatment of the amorphous alloy at this specific temperature leads to the production of the nanocrystalline-amorphous composite. Moreover, Fig. 3c shows the FE-SEM image of the $Al_{86}Cu_6Y_6Co_2$ amorphous sample annealed to 723 K. According to the XRD pattern, the second crystallization onset is [amorphous] → [α-Al + (Al_3Y, $AlCu_3$, $Al_{11}Y_3$, and some unknown phases)]. Based on the chemical analysis of a completely crystallized sample (Fig. 3e and f), white and dark particles were identified as phases containing Al and rich in Al, Cu, Co, and Y elements, respectively. There are homogeneously dispersed fine α- Al and intermetallic phases with sizes less than 50 nm along grain boundaries and inside the grain regions of the alloy. Moreover, the disappearance of the amorphous phase and fcc-Al nanocrystals coarsening can be observed. It has been found that in the Al-TM-RE metallic glasses, the presence of intermetallics between Al-TM and Al-RE has an unpleasant effect on the materials' properties which leads to a decrease in their ductility [25].

Table 2 represents the microhardness results with typical optical images of indentation marks of the as-cast and as-spun specimens of the $Al_{86}Cu_6Y_6Co_2$ alloy. The microhardness amount of $Al_{86}Cu_6Y_6Co_2$ as-spun ribbons following isochronal heating at various temperatures is also observed in Table 2. The results show that $Al_{86}Cu_6Y_6Co_2$ as-spun ribbons with amorphous microstructure reveal higher hardness values than the as-cast sample. A microhardness of about 265 Hv has been achieved for the amorphous melt-spun alloy which is more than three times that of the conventional cast one. Moreover, the hardness of $Al_{86}Cu_6Y_6Co_2$ amorphous alloy alters based on the crystallization reactions, where it increases noticeably (~310 HV) after heating at 623 K (the first crystallization step) and decreases (~285 HV) during the second stage (723 K). According to Table 2, it can be found that the maximum value of the hardness is related to the first crystallization stage with the composite microstructure of nano-sized fcc α-Al phase and an amorphous matrix.

Discussion

Structural study

The XRD pattern of the as-quenched alloy is shown in Fig. 1a. A broad halo confirming the amorphous structure can be observed in the pattern. In some Al-TM-RE systems, a little shoulder may be considered on the wide peak due to the short-range local arrangement of constituents which is not observed in the studied material. Based on the XRD analysis, it can be demonstrated that the $Al_{86}Cu_6Y_6Co_2$ as-spun alloy produced in this work has an amorphous structure. According to the FE-SEM image of the as-spun alloy (Fig. 3a), there is no apparent crystal in the microstructure which approves the amorphous structure of the ribbons. The empirical guidelines of Inoue can be attributed to explaining high GFA in the alloy [26]. Having a multicomponent system with a large atomic size mismatch (i.e., > 12%) and negative heat of mixing contributes to better glass formation in the alloy system. In addition, according to the confusion principle [10], the GFA is high in alloys with more components. In an alloy, the presence of more elements (Cu, Co, Y) leads to a decrease in the stability of the possible crystalline phases which form and suppress the long-range ordered crystalline structures.

Atomic size mismatch and negative heat of mixing between the constituent elements (Al, Cu, Co, and Y) enhance the GFA of the Al alloys because of the influence of Al atoms on dissimilar atoms. The bond Al–TM (TM = Cu and Co) length is noticeably small. Therefore, the molten alloy represents lower shear viscosity and refuses the nucleation process. In addition, the random order of the RE (Y) atoms stabilizes the amorphous structure [8].

There are two specific stages in the crystallization process of $Al_{86}Cu_6Y_6Co_2$ (at. %) amorphous alloy (Fig. 2). However, a small peak can be identified more at the heating rate of 30 $Kmin^{-1}$ between two peaks. As this peak is so close to the first and second specific peaks, its recognition as an individual crystallization stage is associated with uncertainty. According to the XRD result (Fig. 1b), precipitation of fcc α-Al nanoparticles from the amorphous matrix occurs initially. From the positions of the α-Al (cubic lattice) XRD peaks, the lattice parameter can be calculated. The lattice parameter of the annealed ribbons (0.4066) is more than the value for the pure Al (0.4050 nm) indicating an extended solid solution limit. Therefore, high-cooling rates during the melt spinning process enhance the alloying elements in the Al matrix and the primary crystallization of intermetallic phases is avoided.

There are different criteria for studying the crystallization kinetics, thermal stability, and GFA of the

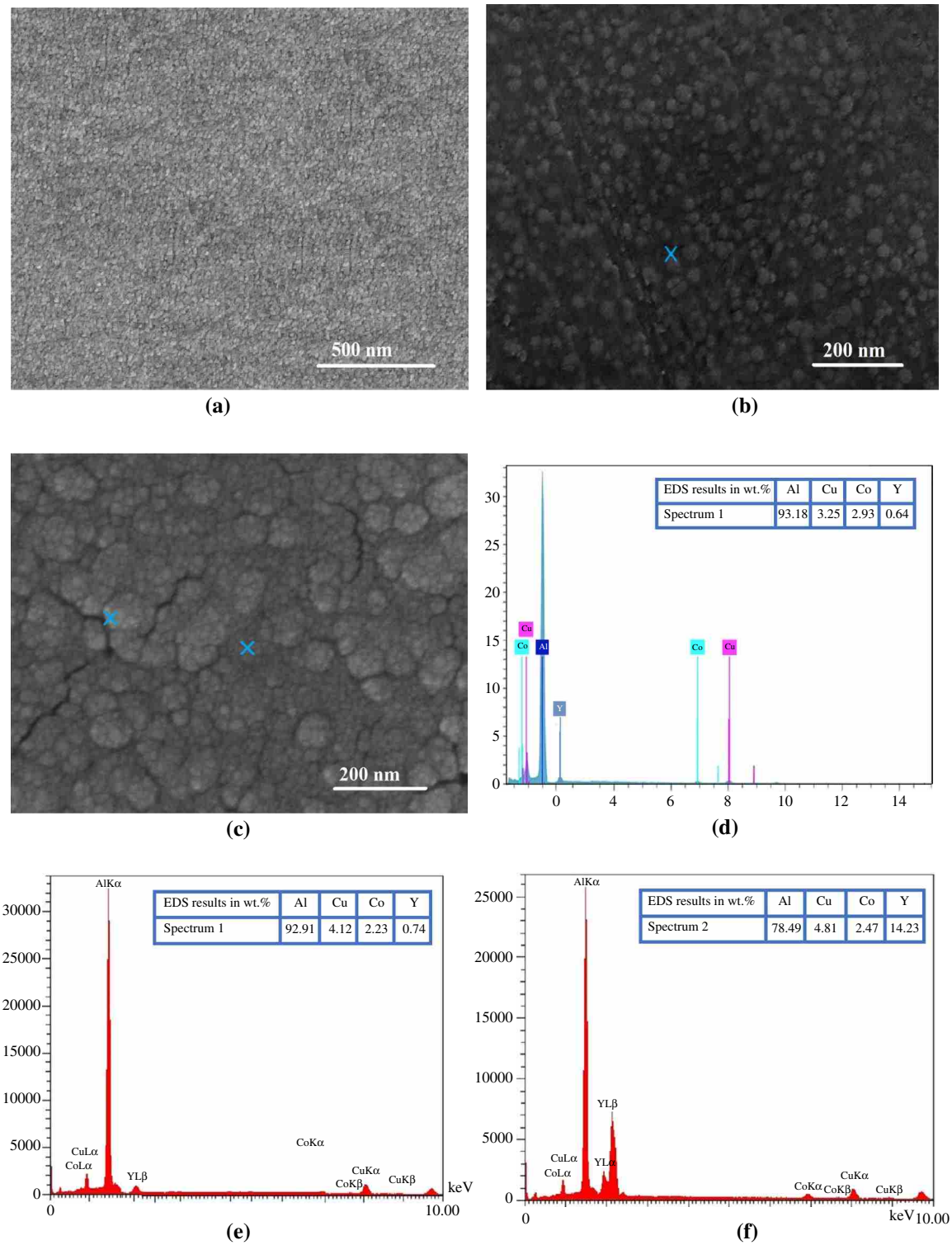

Fig. 3 FE-SEM images show the morphological structure of the $Al_{86}Cu_6Y_6Co_2$ (at. %) alloys for (**a**) as-quenched amorphous alloy and (**b**) alloy heated isochronal to 623 K (a temperature at the end position of the first peak), (**c**) alloy heated to 723 K (at the end position of the second peak), (**d**) EDS pattern of the selected light phase in the (**b**) and (**e** and **f**) EDS patterns of the selected light (spectrum 1) and dark phases (spectrum 2) in (**c**), respectively

Table 2 Hardness (HV) of the $Al_{86}Cu_6Y_6Co_2$ alloy with typical optical images of indentation marks at as-cast, as-quenched and annealed states at 623 K and 723 K related to each DSC reaction

	Hardness/Vickers	Optical images (Indentation marks)
Ingot	84.86 ± 4.23	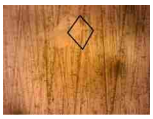
As melt-spun	265.54 ± 12.61	
Annealed at 623 K	310.17 ± 14.35	
Annealed at 723 K	285.08 ± 12.21	

alloy systems. One of the well-defined criteria, supercooled liquid stability [27] is determined by ΔT_{X1} ($T_{X1} - T_g$). The maximum amount of ΔT_{X1} of the $Al_{86}Cu_6Y_6Co_2$ (at. %) amorphous alloy is 26 K (10 $Kmin^{-1}$) and comparable with the 24 K reported for $Al_{86}Cu_6Y_6Co_2$ (at. %) amorphous alloy [17] which implies the $Al_{86}Cu_6Y_6Co_2$ amorphous alloy has high thermal stability. Therefore, the alloy refuses the nucleation and growth processes and represents more GFA. While ΔT_X in the bulk metallic glasses often is > 50 K [17], in the Al metallic glasses is < 30 K. Figure 2 shows a broad exothermic reaction in the first crystallization process with the onset crystallization of 576 K, and reactions are finished at a temperature of about 670 K. The high onset temperature of the alloy can be described by the explained empirical rules [26]. The large Y atoms decrease the diffusion coefficient resulting in more stability of the amorphous structure.

Kinetics of crystallization

Calculation of activation energy

The kinetics effect and thermal stability of the amorphous materials were estimated from the activation energy of crystallization, E_a, by various methods [28–31] including Kissinger, Ozawa, and Augis- Bennet equations.

$$\ln\left(\frac{\beta}{T_p^2}\right) = \left(-\frac{E_a}{RT_p}\right) + C \quad \text{(Kissinger)} \tag{1}$$

$$\ln(\beta) = \left(-\frac{1.0516E_a}{RT_p}\right) + C \quad \text{(Ozawa)} \tag{2}$$

$$\ln\left(\frac{\beta}{T_p - T_0}\right) = \left(-\frac{E_a}{RT_p}\right) + C \quad \text{(Augis and Bennett)} \tag{3}$$

In these equations, β, T_p, T_0, E_a, R, and C are the rate of heating, the temperature of each DSC peak, the initial temperature of DSC analysis, activation energy, universal gas constant (8.314 JK^{-1} mol^{-1}), and a constant value, respectively. E_a implies the required energy to occur in a crystallization process. The larger the activation energy indicates the higher thermal stability. The kinetics of crystallization of the $Al_{86}Cu_6Y_6Co_2$ amorphous ribbons were studied by Kissinger, Ozawa, and Augis- Bennett methods, which have been shown in Fig. 4 which displays excellent linearity. The slope of each plot, which displays excellent linearity, yields the apparent activation energies E_a for the DSC reaction peaks (T_{P1} and T_{P2}) which were reported in Table 3. It is clear that the second crystallization reaction in the $Al_{86}Cu_6Y_6Co_2$ ribbons shows more activation energy than the primary crystallization. It is possibly due to the formation of products with more complicity during the second crystallization stage. In other words, the devitrification of peak 1 is easier than peak 2 according to all three methods indicating the easier phase transition of primary α-Al than intermetallic phases. This may be due to the sluggish movement of the atoms as the result of decreasing diffusion after α-Al phase precipitation. The first crystallization of $Al_{86}Cu_6Y_6Co_2$ amorphous alloy shows relatively high activation energies (Kissinger: 173.4±10.7 $kJ.mol^{-1}$, Ozawa: 174.1±10.2 $kJ.mol^{-1}$, Augis- Bennett: 178.2±12.7 $kJ.mol^{-1}$) and high stability upon crystallization. The results show that all these methods yield approximately similar values of activation energies. Despite this, Augis- Bennett and Ozawa methods represent higher activation energies than those calculated by others for peak 1 and peak 2, respectively. The activation energy for primary crystallization (E_{P1}) of $Al_{86}Ni_8Y_6$ and $Al_{86}Ni_6Y_{4.5}Co_2La_{1.5}$ as-cast ribbons (with similar solute content for the amorphous phase in the present work) evaluated by Kissinger, Ozawa and Augis-Bennett equations are reported in the range of 166–183 $kJ.mol^{-1}$ and 193–207 $kJ.mol^{-1}$, respectively [13].

Crystallized fraction

The fractional area of the DSC exothermic peak can be applied to determine the volume fraction of the

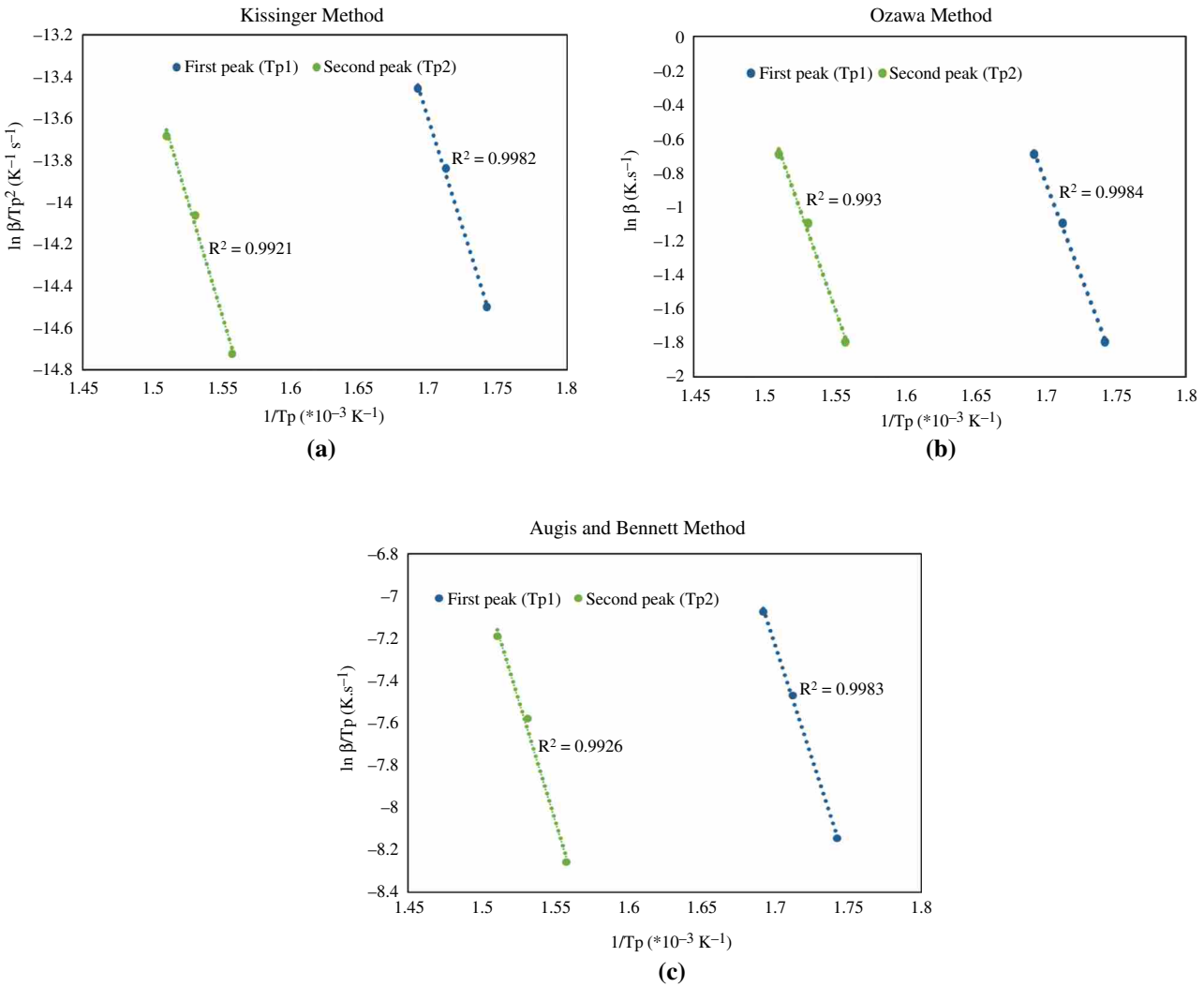

Fig. 4 The first and second crystallization plots of $Al_{86}Cu_6Y_6Co_2$ amorphous alloy; **a** Kissinger, **b** Ozawa and **c** Augis- Bennet

Table 3 Crystallization activation energies of the $Al_{86}Cu_6Y_6Co_2$ alloy has been studied by Kissinger, Ozawa and Augis-Bennett methods

Ea/KJ.mol^{-1}			
Augis-Bennett	Ozawa	Kissinger	Devitrification
178.2 ± 12.7	174.1 ± 10.2	173.4 ± 10.7	T_{P1}
180.4 ± 14.2	185.6 ± 12.3	184.3 ± 14.1	T_{P2}

crystallization α, according to the following equation [32, 33]:

$$\alpha = \frac{\int_{T0}^{T}\left(\mathrm{d}H/\mathrm{d}T\right)\mathrm{d}T}{\int_{T0}^{T}\left(\mathrm{d}H/\mathrm{d}T\right)\mathrm{d}T} \quad (4)$$

In this equation, T_0, T_∞ and dH/dT are the initial temperatures, temperature at the end of each reaction peak and heat capacity of the alloy at constant pressure, respectively. Figure 5a and b shows the volume fraction (α) of the crystallized phases for Peak 1 and Peak 2 of the DSC curve at various heating rates, respectively. A conventional sigmoid order can be observed in all the curves. The crystallization occurs with a smaller rate at low annealing temperature. The nucleation and growth process are conducted the crystallization of the studied amorphous alloy supporting from the sigmoidal *S* type curves which usually consists of three steps [21]: Initially, the crystallization of the alloy is dominated by formation of the nuclei at low volume fractions; therefore, there is a low rate of crystallization process. Then, increasing the volume fraction of the crystallized phase decreases the free energy because of the crystals formation, and interface energy (crystals and matrix) enhances the rate of the crystallization process. Finally, the interface energy reduces which leads to decrease the rate of the crystallization.

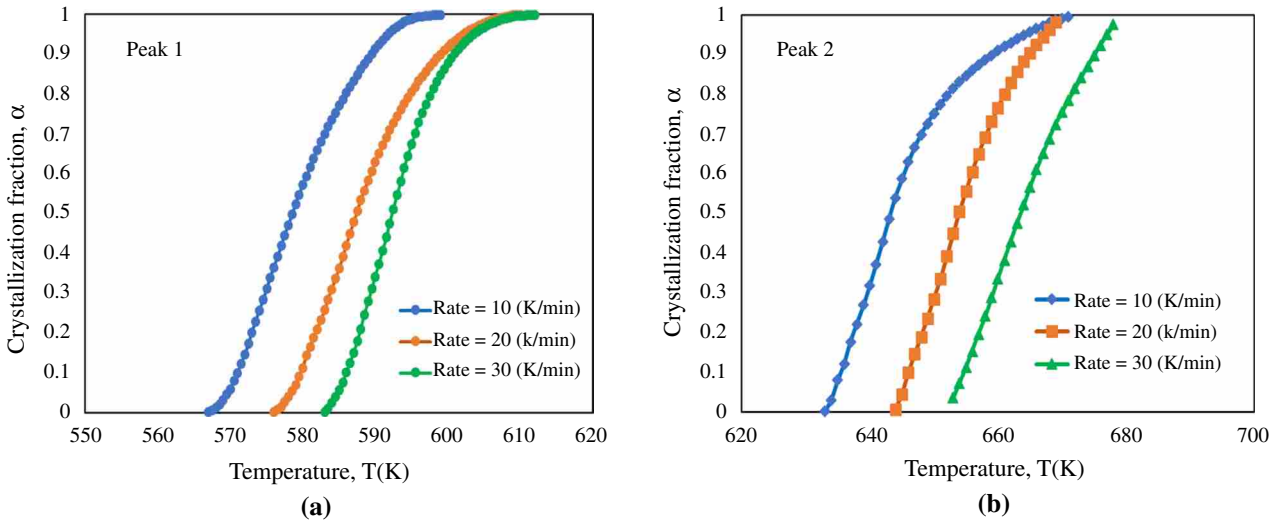

Fig. 5 The crystalized fraction versus crystallization temperature in the amorphous sample (at 10, 20 and 30 Kmin.$^{-1}$ heating rates) for (**a**) peak 1 and (**b**) peak 2

Crystallization mechanism

In order to estimate the local Avrami exponent, n, the Johnson—Mehl—Avrami (JMA) method were applied to study the crystallization kinetics in isothermal condition [20, 34]:

$$\alpha(T) = 1 - \exp\left[-K(t-\tau)^{n}\right] \tag{5}$$

In the equation, α (T) is the degree of crystallization at time t, τ is the time lag, n is Avrami exponent (indicating the crystallization mechanism) and K is an Arrhenius reaction rate which can be obtained from:

$$\mathrm{K}(T) = A\exp\left(-\frac{E_{\mathrm{a}}}{RT}\right) \tag{6}$$

In this equation, A, R, E_{a}, and T are the frequency factor, gas constant, apparent activation energy, and annealing temperature, respectively.

Although the JMA equation has been performed first for the isothermal experiments, it can be applied to the crystallization kinetics study in non-isothermal conditions. At the condition that the nucleation process decreases significantly over time, the JMA equation has been extended by Henderson for the non-isothermal methods [35, 36]:

$$\alpha(T) = 1 - \exp\left[\left(\frac{KT}{\beta}\right)^{n}\right] \tag{7}$$

Which can be written as:

$$\ln[-\ln(1-\alpha)] = -n\ln\beta + \ln K(T) \tag{8}$$

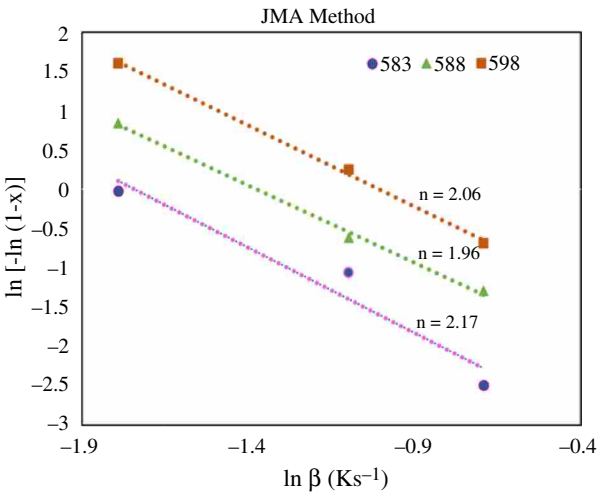

Fig. 6 The first crystallization process of the $Al_{86}Cu_6Y_6Co_2$ alloy at different temperatures determined by the JMA equation

Table 4 Non-isothermal crystallization parameters for the primary stage in $Al_{86}Cu_6Y_6Co_2$ alloy at different temperatures

	Temperature/K			
	583	588	598	
$\overline{n} = 2.0650.16$	2.170	1.962	2.062	Avrami exponent n
$\overline{K} = 0.072 \pm 0.031$	0.023	0.067	0.126	Reaction constant K(T)

The slope of plotting ln[-ln(1-α)] versus lnβ in Fig. 6 at various temperatures can be used in order to determine the Avram exponent (n). Table 4 reports the reaction constant and mean value of the crystallization index (n) for the first crystallization of the $Al_{86}Cu_6Y_6Co_2$ amorphous ribbons at

various rates of heating. The value of n can be calculated from [37]:

$$n = a + bc \tag{9}$$

In this equation, a, b and c are the index of nucleation, growth dimensionality, and index of growth, respectively. It was reported that the first reaction of most Al–TM–RE metallic glasses is diffusion-controlled growth in which diffusion of the solute atoms has an important effect on the type of the primary phase [17]. Therefore, considering $c = 0.5$ in the case that growth is controlled by diffusion, Eq. 9 can be represented as $n = a + 0.5b$. Avrami exponent has been used to determine the mechanism of nucleation and growth [36]. According to Table 4, the average amount of n for the first crystallization stage in the $Al_{86}Cu_6Y_6Co_2$ alloy is ~ 2.01 which reveals the crystallization controlled by three-dimensionally diffusion mechanisms with decreasing rate of nucleation. It is reported that the composition has an important effect on the amounts of E and n where, in some amorphous Al alloys, the Kissinger method yields the activation energies and Avrami exponent in the range of 146–317 kJmol^{-1} and 1.6–5.0 for the primary crystallization, respectively [11]. Although it is reported that the nucleation process conducts the formation of a primary nano-sized phase [39], the growth process determines the size and morphology of the precipitated phases. Large RE (Y) atoms with small diffusivity from solute atoms suppress the growth process and the movement of atoms decreases even more as a result of impingement. This leads to an increase in the content of TM (Co and Cu) and RE (Y) elements and redistribution of the solute atoms in the amorphous matrix after primary crystallization. Therefore, fcc-Al nanocrystals are formed in the glassy matrix during the primary crystallization.

Hardness changes

In this study, a microhardness test was used on the $Al_{86}Cu_6Y_6Co_2$ alloy at as-cast, as-spun, and annealed states. Table 2 also reports the microhardness values of the heat-treated ribbons at temperatures corresponding to each DSC reaction. The amorphous alloy shows a higher hardness value (265.54 ± 12.61 HV) more than three times that of as-cast one (84.86 ± 4.23 HV) with coarse microstructure. Moreover, the extended solubility of elements in the matrix due to rapid solidification process, which leads to the presence of metastable crystals and formation of metallic glasses, can contribute to the enhanced microhardness of the rapidly solidified ribbons. The hardness of 250 Hv has been also reported for $Al_{88}Y_2Ni_{10-x}M_x$ (M = Fe or Co) amorphous alloys with about similar solute content for the amorphous phase in the present work [40].

It is obvious the hardness of amorphous ribbon (265.54 ± 12.61 HV) changes largely after heat treatment of the amorphous $Al_{86}Cu_6Y_6Co_2$ ribbons related to the different crystallization products which are shown in Fig. 1 (XRD patterns). This is due to the enrichment of the amorphous matrix with solute content, which is an important factor in the hardening during annealing [38, 40]. The amorphous ribbon after isochronal annealing at 623 K shows enhanced microhardness (310.17 ± 14.35 HV) indicating the fcc-Al nanocrystals influence significantly the hardness of the amorphous alloy. In the other words, the amorphous ribbons after heat treatment at the temperature corresponding to the end position of the first reaction peak show a gradual increase in the microhardness, attributed to the crystallization onset: [amorphous] → [amorphous + α-Al]. In addition to the enhanced solute content of the residual amorphous matrix, precipitation hardening due to homogeneously precipitated α-Al nanocrystals enhances the hardness after the first reaction. Also, the hardness of the $Al_{86}Cu_6Y_6Co_2$ amorphous alloy decreases (285.08 ± 12.21 HV) after the second DSC reaction. Formation of some weak intermetallic compounds (e.g. $Al_{11}Y_3$), Al particle growth, and crystallization of the amorphous matrix completely may contribute to decreasing the hardness after this stage. The mechanical properties of the Al metallic glasses after heat treatment depend strongly on the composition and content of solutes for the amorphous phase. S. F. Chen et.al reported the hardness of 363 and 379 Hv for the $Al_{87}Y_8Ni_5$ and $(Al_{87}Y_8Ni_5)_{99}Ce_1$ ribbons, respectively. It was found that the hardness increased sharply after heat treatment to the second crystallization temperature (T_{x2}), but decreased after the third crystallization temperature (T_{x3}) [41].

Conclusions

The non-isothermal kinetics analysis was applied to study the thermal stability, mechanical properties, and mechanisms of the crystallization of the $Al_{86}Cu_6Y_6Co_2$ (at. %) metallic glass. The rapidly solidified ribbons show high thermal stability during the annealing-induced crystallizations which start at 576 K and 20 Kmin^{-1} indicating high thermal stability of the amorphous alloy. There are two stages of crystallization for the studied alloy. Glass transition temperatures (T_g) can be observed prior to the first reaction temperatures (T_{x1}) in the amorphous alloy. The nano-sized fcc-Al crystals and different intermetallic phases formed from the residual amorphous matrix are the products of the primary (623 K) and second step (723 K) crystallization, respectively. In a completely crystallized sample, the homogeneously distributed fine α- Al and intermetallic phases rich in Al, Cu, Co, and Y elements (size less than 50 nm) were formed along the grain

boundaries and inside the grain regions. The activation energies of the first exothermic peak have been obtained by Kissinger (173.4 ± 10.7), Ozawa (174.1 ± 10.2), and Augis-Bennett (178.2 ± 12.7) methods. All thermodynamic methods yield reliable values which are close to each other. The primary crystallization of the as-spun ribbons with relatively high activation energy indicates good stability against crystallization. The average value of n is about 2.1 which shows the crystallization process is controlled by a 3-D diffusional growth with reducing nucleation. In addition, the hardness values of the as-spun amorphous alloy demonstrate significant improvement after the devitrification. The fcc α-Al nanocrystals precipitated in the glassy matrix are an important factor in the hardening of the $Al_{86}Cu_6Y_6Co_2$ alloy during the primary crystallization. However, the α-Al nanoparticles growth, weak intermetallic phase formation, and complete crystallization of the amorphous matrix may contribute to decreasing the microhardness after the second crystallization stage.

Author contributions **M. Salehi** helped in supervision, conceptualization, methodology, formal analysis, validation, writing—original draft preparation, writing—reviewing and editing; **S.G. Shabestari** contributed to conceptualization, methodology, reviewing and editing; **M. Dadashi** was involved in formal analysis, investigation, validation.

Declarations

Conflicts of interest There is no conflict of interest with regard to the submitted manuscript.

References

1. Öztürk S, Sünbül E, İcin K. Effects of melt spinning process parameters and wheel surface quality on production of 6060 aluminum alloy powders and ribbons. Trans Nonferrous Met Soc China. 2020. https://doi.org/10.1016/S1003-6326(20)65287-6.
2. Gancarz T, Dobosz A, Bogno AA, Cempura G, Schell N, Chulist R, Henein H. Characterization of rapidly solidified Al-Mg-Sc alloys with Li addition. Mater Charact. 2021. https://doi.org/10.1016/j.matchar.2021.111290.
3. Yang Y, Licavoli JJ, Anders PG. Improved strengthening in supersaturated Al-Sc-Zr alloy via melt-spinning and extrusion. J Alloys and Compd. 2020;826:154185. https://doi.org/10.1016/j.jallcom.2020.154185.
4. Abboud JH, Kayitmazbatir M. Microstructural evolution and hardness of rapidly solidified hypereutectic Al-Si surface layers by laser remelting. Adv Mater Process Technol. 2022;8(4):4136–55. https://doi.org/10.1080/2374068X.2022.2037352.
5. Li W, Yang L, Zhang YG, Kong LT, Li JF. Influences of Si addition on the thermal stability and crystallization behavior of Al-Y binary amorphous alloys. J Alloy Compd. 2021. https://doi.org/10.1016/j.jallcom.2021.159816.
6. Sharma A, Zadorozhnyy V. Review of the recent development in metallic glass and its composites. Metals. 2021. https://doi.org/10.3390/met11121933.
7. Berezner AD, Fedorov VA, Zadorozhnyy MY. Relaxation behavior of an Al-Y-Ni-Co metallic glass in as-prepared and cold-rolled state. J Alloys Compd. 2022. https://doi.org/10.1016/j.jallcom.2022.166313.
8. Rios CT, Suriñach S, Baró MD, Bolfarini C, Botta WJ, Kiminami CS. Glass forming ability of the Al–Ce–Ni system. J Non-Cryst Solids. 2008. https://doi.org/10.1016/j.jnoncrysol.2008.04.035.
9. Wang SH, Bian XF. Effect of Si and Co on the crystallization of Al–Ni–RE amorphous alloys. J Alloys Compd. 2008. https://doi.org/10.1016/j.jallcom.2006.11.056.
10. Cuevas FG, Lozano-Perez S, Aranda RM, Caballero ES. Crystallization of amorphous Al-Sm-Ni-(Cu) alloys. Intermetallics. 2008. https://doi.org/10.1016/j.intermet.2019.106537.
11. Shen Y, Perepezko JH. Al-based amorphous alloys: Glass-forming ability, crystallization behavior and effects of minor alloying additions. J Alloy Compd. 2017. https://doi.org/10.1016/j.jallcom.2016.11.079.
12. Wang Y, Liu Y, Li Y, An B, Cao G, Jin S, Sun Y, Wang Y. Crystallization of Al-based amorphous alloys in good conductivity solution. J Mater Sci Technol. 2014. https://doi.org/10.1016/j.jmst.2014.10.003.
13. Sahu A, Maurya RS, Laha T. Non-isothermal crystallization behavior of $Al_{86}Ni_8Y_6$ and $Al_{86}Ni_6Y_{4.5}Co_2La_{1.5}$ melt-spun ribbons, milled ribbon particles and bulk samples consolidated by spark plasma sintering. Thermochimica Acta. 2020;684:178486. https://doi.org/10.1016/j.tca.2019.178486.
14. Kim DH, Kim WT, Kim DH. Formation and crystallization of Al–Ni–Ti amorphous alloys. Mater Sci Eng A. 2004. https://doi.org/10.1016/j.msea.2004.04.016.
15. Hyun JI, Kim CI, Nam SW, Kim WT, Kim DH. Nanoscale phase separation and microstructure evolution during crystallization in Al-Si-Ni amorphous alloy. Mater Des. 2020. https://doi.org/10.1016/j.matdes.2020.108719.
16. Li FC, Liu T, Zhang JY, Shuang S, Wang Q, Wang AD, Wang JG, Yang Y. Amorphous- nanocrystalline alloys: fabrication, properties, and applications. Mater Today Adv. 2019. https://doi.org/10.1016/j.mtadv.2019.100027.
17. Salehi M, Shabestari SG, Boutorabi SMA. Nano-crystal development and thermal stability of amorphous Al–Ni–Y–Ce alloy. J Non-Cryst Solids. 2013. https://doi.org/10.1016/j.jnoncrysol.2013.04.059.
18. Munoz-Morris MA, Surinach S, Varga LK, Baro MD, Morris DG. Crystallization of a Al–4Ni–6Ce glass and its influence on mechanical properties. Scr Mater. 2002. https://doi.org/10.1016/S1359-6454.
19. Kim HS, Hong SI. A model of the ductile-brittle transition of partially crystallized amorphous Al-Ni-Y alloys. Acta Mater. 1999. https://doi.org/10.1016/S1359-6454(99)00088-9.
20. Huang ZH, Li JF, Rao QL, Zhou YH. Primary crystallization of Al–Ni–RE amorphous alloys with different type and content of RE. Mater Sci Eng A. 2008. https://doi.org/10.1016/j.msea.2007.12.027.
21. Dong Q, Song P, Tan J, Qin XM, Li CJ, Gao P, Feng ZX, Calin M, Eckert J. Non-isothermal crystallization kinetics of a Fe-Cr-Mo-B-C amorphous powder. J Alloys Compd. 2020. https://doi.org/10.1016/j.jallcom.2020.153783.
22. Wang X, Deng L, Xie J, Liang D. Non-isothermal kinetic parameters and models of crystallization for amorphous Fe–Co–Nb–Cu–B alloys. Physica B. 2013. https://doi.org/10.1016/j.physb.2012.09.060.
23. Perepezko JH, Hebert RJ. Amorphous aluminum alloys—synthesis and stability. JOM. 2002;54(3):34–9. https://doi.org/10.1007/BF02822618.
24. Busch R, Kim YJ, Johnson WL. Thermodynamics and kinetics of the undercooled liquid and the glass

transition of the $Zr_{41.2}Ti_{13.8}Cu_{12.5}Ni_{10.0}Be_{22.5}$ alloy. J Appl Phys. 1995;77(8):4039–43. https://doi.org/10.1063/1.359485.
25. Muñoz-Morris MA, Suriñach S, Varga LK, Baro MD, Morris DG. The influence of composition and low temperature annealing on hardness and ductility of rapidly solidified Al–Ni–Ce alloys. Scr Mater. 2002;47(1):31–7. https://doi.org/10.1016/S1359-6462(02)00093-3.
26. Inoue A. Stabilization of metallic supercooled liquid and bulk amorphous alloys. Acta Mater. 2000. https://doi.org/10.1016/S1359-6454(99)00300-6.
27. Song K, Bian XF, Lv X, Guo J, Li G, Xie M. Correlation between glass-forming ability, thermal stability, and crystallization kinetics of Cu-Zr-Ag metallic glasses. Mater Sci Eng A. 2009. https://doi.org/10.1016/j.msea.2008.11.043.
28. Kissinger HE. Variation of peak temperature with heating rate in differential thermal analysis. J Res Natl Bur Stand. 1956;57(4):217. https://doi.org/10.6028/jres.057.026.
29. Kissinger HE. Reaction kinetics in differential thermal analysis. Anal Chem. 1957;29(11):1702–6. https://doi.org/10.1021/ac60131a045.
30. Fatmi M, Ghebouli B, Ghebouli MA, Chihi T, Abdul Hafiz M. The kinetics of precipitation in Al-2.4wt% Cu alloy by Kissinger, Ozawa, Bosswel and Matusita methods. Phys B: Condensed Matter. 2011;406(11):2277–80. https://doi.org/10.1016/j.physb.2011.03.053.
31. Augis J, Bennett J. Calculation of the Avrami parameters for heterogeneous solid state reactions using a modification of the Kissinger method. J Therm Anal Calorim. 1978. https://doi.org/10.1007/BF01912301.
32. Paul T, Loganathan A, Agarwal A, Harimkar SP. Kinetics of isochronal crystallization in a Fe-based amorphous alloy. J Alloy Compd. 2018;753:679–87. https://doi.org/10.1016/j.jallcom.2018.04.133.
33. Lu XF, Hay JN. Isothermal crystallization kinetics and melting behaviour of poly(ethylene terephthalate). Polymer. 2001;42(23):9423–31. https://doi.org/10.1016/S0032-3861(01)00502-X.
34. dos Santos DS, dos Santos DR. Crystallization kinetics of Fe–B–Si metallic glasses. J Non-Cryst Solids. 2002;304(1–3):56–63. https://doi.org/10.1016/S0022-3093(02)01004-9.
35. Henderson DW. Thermal analysis of non-isothermal crystallization kinetics in glass forming liquids. J Non-Cryst Solids. 1979. https://doi.org/10.1016/0022-3093(79)90169-8.
36. Henderson DW. Experimental analysis of non-isothermal transformations involving nucleation and growth. J Therm Anal. 1979. https://doi.org/10.1007/BF01903656.
37. Ranganathan S, Von Heimendahl M. The three activation energies with isothermal transformations: applications to metallic glasses. J Mater Sci. 1981;16(9):2401–4. https://doi.org/10.1007/BF01113575.
38. Hong SJ, Kim TS, Kim HS, Kim WT, Chun BS. Microstructural behavior of rapidly solidified and extruded Al-14wt%Ni-14wt%Mm (Mm, misch metal) alloy powders. Mater Sci Eng: A. 1999;271(1–2):469–76. https://doi.org/10.1016/S0921-5093(99)00317-2.
39. Zhang Z, Witkin D, Lavernia E J. Crystallization behavior of a gas atomized $Al_{85}Ni_{10}La_5$ amorphous alloy. J Non-Cryst Solids. 2005;351(19–20):1646–52. https://doi.org/10.1016/j.jnoncrysol.2005.04.055.
40. Jin Y, Inoue A, Kong FL, Zhu SL, Al-Marzouki F, Greer AL. Ultrahigh thermal stability and hardness of nano-mixed fcc-Al and amorphous phases for multicomponent Al-based alloys. J Alloy Comp. 2020;832:154997. https://doi.org/10.1016/j.jallcom.2020.154997.
41. Chen S-F, Chen C-Y, Lin C-H. Insight on the glass-forming ability of Al–Y–Ni–Ce bulk metallic glass. J Alloy Comp. 2015;637:418–25. https://doi.org/10.1016/j.jallcom.2015.02.217.